metals

MDPI

Article

The Effect of Energy Parameters of Power Sources on the Structure and Properties of Permanent Joints at Manual Arc Welding

Dmitry P. Il'yashchenko [1,2,*], Dmitry A. Chinakhov [3] and Elena V. Lavrova [4]

[1] Yurga Technological Institute, National Research Tomsk Polytechnic University, Building 30, Lenin Ave., 634050 Tomsk, Russia
[2] Institute of Strength Physics and Materials Science of Siberian Branch Russian Academy of Sciences, Academic Ave., 2/4, 634055 Tomsk, Russia
[3] Aircraft Faculty, Novosibirsk State Technical University, Novosibirsk 20 K. Marksa Prospekt, 630073 Novosibirsk, Russia
[4] UNIST, Pryazovskyi State Technical University, Universitetskaya 7, 287555 Mariupol, Russia
* Correspondence: mita8@tpu.ru

Abstract: The study presents the results of the research into the effect of the dynamic properties of inverter and diode power sources of welding arc power supply on the stability of melting and transfer of electrode metal into the weld pool. The principal energy parameters of the power source include the rates of rise and fall of short-circuit current, the ratio of arc burning current to short-circuit current, and other related factors. It has been demonstrated that an increase in the rate of change of these parameters within one welding mode microcycle alters the properties of heat and mass transfer, increases the frequency of electrode metal droplet transfer, reduces the size of transferred droplets in the weld pool and the duration of their stay on the electrode end under the influence of the high temperature of the welding arc, and the duration of short circuits. The increase in the mass fraction of alloying elements at their transition from the coated electrode to the weld metal is demonstrated to depend on the rate of change of the main energy parameters of one welding mode microcycle of the inverter power source in comparison with the diode rectifier. An enhancement in the structural integrity and properties of permanent joints during welding has been observed when using an inverter power source for the welding arc with high dynamic properties.

Keywords: welding arc power source; welding mode microcycle; manual arc welding; steel; structure; properties of welded joints

Citation: Il'yashchenko, D.P.; Chinakhov, D.A.; Lavrova, E.V. The Effect of Energy Parameters of Power Sources on the Structure and Properties of Permanent Joints at Manual Arc Welding. *Metals* **2024**, *14*, 759. https://doi.org/10.3390/met14070759

Academic Editor: Roberto Montanari

Received: 14 May 2024
Revised: 14 June 2024
Accepted: 22 June 2024
Published: 27 June 2024

1. Introduction

Inverter power sources for welding have become prevalent due to the expediency with which the parameters of the welding mode can be controlled. These include the rate of short-circuit current rise and fall and the ratio of values of arc burning current and short-circuit current, among other parameters, which lead to the transfer of electrode metal drop.

The authors of [1] propose technical solutions designed to enhance the welding process by eliminating the short-circuiting of the arc gap. These solutions are based on the development of special algorithms for controlling the operation of inverter welding current sources. Paper [2] examines the primary trends in the development of equipment for fusion arc welding and their impact on the stability of the welding process. The authors of [3] establish the reduction of the unfavorable factor of inverter-based welding, both for the qualitative and quantitative components of welding aerosol. Studies [4–13] present the research results on the stability of the welding process in the system "power source—welding arc". Papers [14–18] contain analysis of how the modern elementary base of welding equipment affects the efficiency of the welding process with a fusion electrode. This is equally

applicable to the analysis of heat and mass transfer properties during manual arc welding with a flux-coated electrode. This necessitates the complex theoretical and experimental studies of welding processes, including the melting, transfer of the electrode's metal, and crystallization of weld metal from the melt during the formation of welded joints and clad coatings.

The results of the conducted research will establish dependence between the properties of heat and mass transfer of electrode metal droplets, the heat content of the weld pool, and the structure of the weld, as well as the physical, mechanical, and operational properties of the welded metal joints. This will enable the formulation of recommendations for improving the operational properties of welded metal structures when using inverter rectifiers.

When welding metal structures, the production of which is difficult to mechanize, automate, and robotize, manual metal arc welding with coated electrodes (MMAW) is one of the leading manufacturing processes. This is explained by its flexibility, simplicity, versatility, and lower costs of auxiliary operations and equipment, especially in unprepared conditions [1,2].

The objective of this study is to evaluate the influence of the dynamic properties of inverter and diode power sources on the stability of melting and transfer of electrode metal into the weld pool, which are the main indicators of heat and mass transfer and affect the structure and mechanical properties of the formed permanent joints.

The dynamic properties of power sources are understood as the change of the welding mode's main energy parameters over time. These changes occur in the process of melting and transferring electrode metal into the weld pool within one welding microcycle [1–13]. The physical essence of the process of forming a permanent MMAW joint can be explained by the scheme presented in Figure 1.

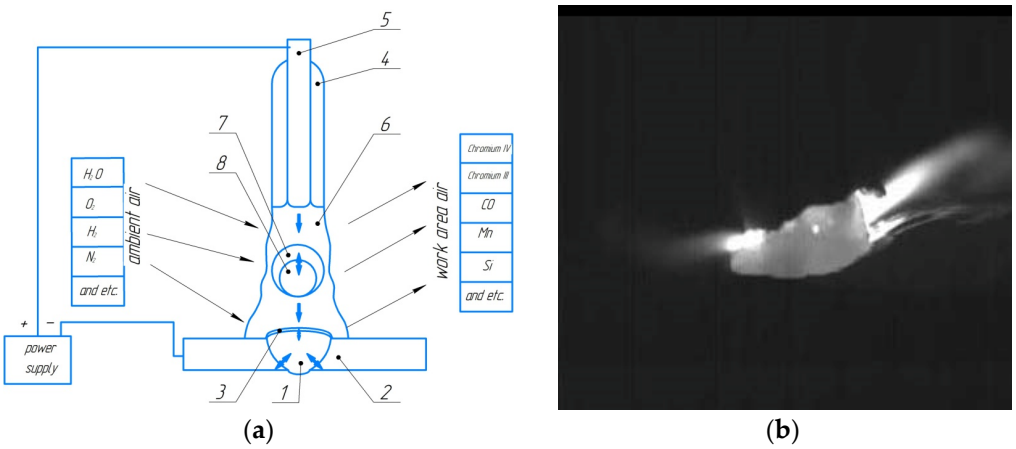

(**a**) (**b**)

Figure 1. The essence of the MMAW process, reprinted from Ref. [3]: (**a**) is a block diagram of electrode melting and seam metal formation; (**b**) is an image of the process of electrode-metal droplet transfer. 1: clad metal; 2: base metal; 3: slag; 4: electrode flux; 5: metal electrode rod; 6: gas atmosphere; 7: slag phase of the molten electrode droplet; 8: metal phase of the molten electrode droplet.

The electrode melting process can be divided into three stages (Figure 1), which differ in temperature, geometric, hydrodynamic, and physicochemical properties [19–26].

The initial stage is the beginning of electrode melting. At this stage, the arc length, resistance of the interelectrode gap, arc voltage, and energy losses for radiation into the environment are maximized. The liquid metal at the electrode end is heated by the arc, reaching a temperature of at least 6000 K [14,17] and is held at the electrode end by surface tension, which is greater than gravitational forces. However, surface tension gradually decreases due to the increase in temperature of the metal and the appearance of a slag film on it (the percentage of constituents can vary from 0 to 100%). During heating, there occur processes such as the dissociation of electrode coating components, water evaporation, and

interaction of charge materials in the solid state [19]. The melting of the electrode generates the electrode metal droplets covered with a slag film (7 and 8 in Figure 1).

The second stage is the transfer of metal from the electrode to the weld pool. It can occur by tearing off droplets from the electrode under the influence of the pinch effect or by overflowing the droplet, resulting in a short circuit. The authors of [20,21] found that the physicochemical reactions during welding almost completely end at the droplet stage when there is intensive interaction of the droplets with the slag and gas.

The third stage involves the formation of the weld pool (Figure 1). One of the characteristic features of the arc welding process is the brief changes in current magnitude at all stages of the welding cycle. The amplitude of the welding current varies randomly, both in the duration of transient processes and in the frequency of their manifestations. Consequently, the dynamic properties of the welding power source, i.e., its ability to respond quickly to such disturbances and provide stability of the welding current, are the determining factors for the efficiency and quality of the welding process.

Processes [27] occurring in the welding zone have a characteristic duration ranging from 0.1 μs to 0.1 s (Figure 2). Therefore, the operational properties of the deposited metal can be improved by increasing the transfer coefficient of alloying elements from covered electrodes, minimizing losses of alloying elements into the slag and gas components, as well as by thermally affecting the chemical composition of the electrode metal droplet.

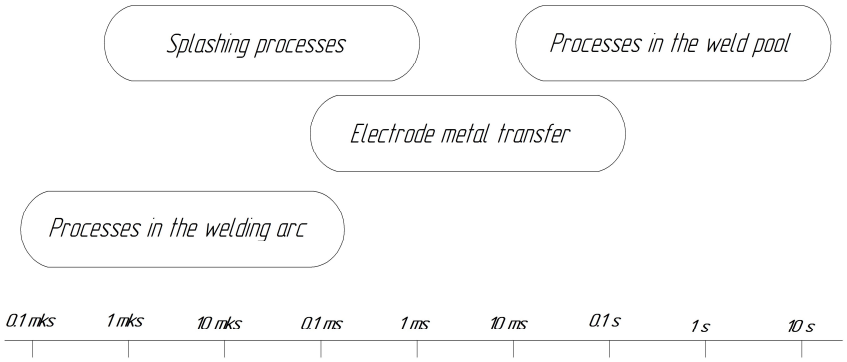

Figure 2. The duration of processes occurring in the weld pool and electric arc.

The works [2,4,6,12,21–23,27–32] argue that reducing the size of electrode droplets leads to an increase in the total surface area of their contact with the environment and results in deoxidation, alloying, oxidation, and gas dissolution. However, a reduction in the droplet existence time (droplet size) results in an increase in the intensity of metallurgical processes. Study [21] reports that the specific surface area of electrode droplets is approximately 5–22 times higher than the specific surface area of the welding pool. Moreover, the specific rate of metal oxidation of electrode droplets is approximately 39 times higher than the specific rate of metal oxidation of the welding pool. Research [22] established that chemical reactions during welding almost entirely finish at the stage of droplet formation, during which there is an intense interaction between droplets, slag, and gas.

The efficiency of transferring chemical elements from welding materials to the weld metal is a relevant issue in welding production. Studies on the kinetics of melting and transfer of electrode metal during arc welding have been conducted in the works by Erokhin A. A. [22], Mazel A. G. [20], Pokhodny I. K. [23], Shatilo S. P. [19], Vaz C. T. [33,34], Rodríguez Jorge V. [35], Chen J. H. [36], Brandi S. [37], Lancaster J. F. [38,39], and others [40,41], who have shown that:

1. The majority of the metal, approximately 85% [2], is transferred in the form of droplets;
2. The size and shape of the droplets, as well as the frequency of their transfer, depend on the thermophysical properties of the electrode metal, the composition of the coating, the thickness of the coating, the diameter of the electrode, the welding regime, the polarity, and the relationship of forces acting on the molten electrode metal at various stages of melting and transfer.

3. The stability of the welding process depends on the nature of metal transfer [1–13,20–23].

Metallurgical reactions during fusion welding are characterized by the following [19–23]:

Physico-chemical processes that occur in the welding zone as a result of the interaction between molten metal, welding fluxes, and gases;

- Higher rates of seam metal cooling and crystallization;
- Phase transformations of the base metal in the heat-affected zone.

These processes take place throughout the entire arc welding process, from the melting of the electrode to the transition of the molten metal drop through the arc gap to the weld pool. The metallurgical reactions in the electrode-drop-weld pool system differ from those in steel-making furnaces, and the specific features that affect these reactions and their outcome in MMAW are:

1. The small volume of the weld pool and the relatively large number of reactive phases present within it;
2. High temperatures within the welding arc (up to 7000 °C) leading to overheating of the molten material within the pool;
3. The movement of liquid metal, intense mixing of molten materials, and continuous flow of metallurgical processes within the pool;
4. Rapid cooling and solidification rates of deposited metal.

It has been found in [42,43] that as arc power increases, the mass of deposited metal and slag decreases and the amount of welding fumes increases, as confirmed by data from [3,8,44–48].

2. Methodology

There has been comprehensive theoretical and experimental research into the issues. The theoretical studies included: mathematical calculations of the size of transferred electrode droplets, determination of the thermal content of electrode droplets, and heat input into the product. The experimental studies consisted of laboratory experiments, including oscillography of current in the welding circuit, measurement of arc voltage between the electrode and the product, thermal imaging of the thermal fields during welding, macroscopic and microscopic examination of welded joint sections, determination of mechanical properties of welds, and investigation of the effect of the dynamic properties of power sources using various methods of energy conversion (diode rectifiers and inverter rectifiers) on the arc welding process and the properties of welded joints.

To conduct a comprehensive study, welded samples were obtained using different types of equipment, including the Nebula 315 inverter rectifier (Nebula, Nanjing, China) and the VD-306E diode rectifier.

To ensure the required level of study reliability, 3 samples were produced for each test. The samples for the study were made of steels of different grades (steel 09G2S, the main steel for pipelines; carbon steel 45; and 12X18N10T steel used for items operating in aggressive environments) to analyze the influence of dynamic properties of different power sources on the structure and properties of welded joints.

1. A pipe of steel 09G2S (joint type C17) with dimensions of 159 × 6 mm was welded with the following parameters: root pass was conducted with LB-52U (d = 2.6 mm) electrode at a welding current of 50–60 A; filling was conducted with LB-52U (d = 3.2 mm) electrode at a welding current of 80–90 A.
2. Welding of 10 mm-thick plates made of steel 45 (joint type C17) was carried out using the following welding technique (Figure 3): the welding was performed in four layers with electrodes. The root pass was conducted with UONI 13/55 electrodes (d = 3 mm) at a welding current of 80–90 A. The filling was conducted with UONI 13/55 electrodes (d = 4 mm) at a welding current of 120–130 A. Before welding, the parts were preheated to 300 °C and then slowly cooled with asbestos fiber insulation until they were completely cooled.

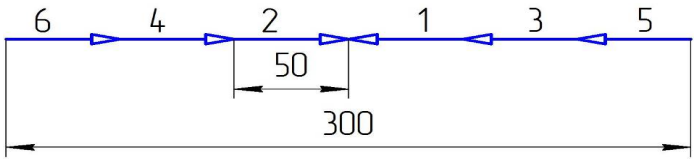

Figure 3. The scheme of welding seams.

3. Welding of 3 mm-thick plates made of 12H18N10T steel (joint type C7) was carried out with CL11 electrodes of 08H20N9G2B type (d = 3 mm) at a welding current of 70–80 A.

Mechanical tests of welded samples were carried out in accredited chemical and metal science laboratories of Kuzbassstekhenergo research and information center.

3. Research Results

The studies have been conducted to investigate the effect of droplet transfer parameters on the size of transferred electrode metal droplets in MMAW. In the course of investigating electrode metal transfer, the following assumptions were incorporated into the mathematical model [1]: the arc column is stationary and coaxial with the electrode, and the molten metal drop has the shape of a segment or a ball. Assuming that the end of the electrode drop has the shape of a spherical segment with a base equal to the cross-section of the electrode, its mass can be calculated using the formula [49]:

$$m = \frac{\pi\gamma}{3}\left[2 \cdot R^3 + (2R^2 + r_0^2)\sqrt{R^2 - r_0^2}\right] \cdot 10^{-3}, \quad (1)$$

where m is the mass of the droplet, γ is the density of the liquid metal (g/mm^3), R is the radius of curvature of the drop surface (mm), and r_0 is the radius of the electrode rod (mm).

On the other hand, the mass of transient droplets during short circuits [2,50,51] can be estimated using a third-order regression equation:

$$m = a \cdot \tau_{s/c}^3, \quad (2)$$

where $\tau_{s/c}$ is the residence time of the droplet at the end of the electrode, s; a is the coefficient 0.33×10^{-4} g/s^3.

Formulas (1) and (2) and the Cardano formula [52] yield the radius of the surface curvature of the electrode droplet, according to the formula [53]:

$$R = \sqrt[3]{\begin{array}{l}\frac{-1}{27} \cdot \left(\frac{-\pi\cdot\gamma\cdot r_0^2}{4\cdot a\cdot \tau_0^3\cdot 10^3}\right)^3 + \left(\frac{-3a\cdot\tau_{\bar{c}}^3\cdot 10^3}{8\cdot\pi\cdot\gamma} + \frac{\pi\cdot\gamma\cdot r_0^2}{24\cdot a\cdot\tau_{s/c}^3\cdot 10^3}\right) - \\ -\sqrt{\frac{2}{27}\left(\frac{-\pi\cdot\gamma\cdot r_0^3}{4\cdot a\cdot\tau_{s/c.}^3\cdot 10^3}\right)^3 + \left(\frac{-3a\cdot\tau_{s.c.}^3\cdot 10^3}{8\cdot\pi\cdot\gamma} + \frac{\pi\cdot\gamma\cdot r_0^2}{24\cdot a\cdot\tau_{s/c.}^3\cdot 10^3}\right)\cdot\frac{1}{4} - \frac{1}{27^2}\cdot\left(\frac{-\pi\cdot\gamma\cdot r_0^2}{4\cdot a\cdot\tau_{s/c.}^3\cdot 10^3}\right)^6} + \\ + \frac{\pi\cdot\gamma\cdot r_0^2}{12\cdot a\cdot\tau_{s/c.}^3\cdot 10^3}.\end{array}} \quad (3)$$

Or simplified variant:

$$R = \sqrt[3]{-\frac{1}{27}\cdot c^3 + \left(B - \frac{c}{6}\right)} - \sqrt{\frac{2}{27}\cdot c^3 + \frac{1}{4}\left(B - \frac{c}{6}\right) - \frac{1}{729}\cdot c^6} - \frac{c}{3}, \quad (4)$$

where $c = \frac{-\pi\cdot\gamma\cdot r_0^2}{4a\cdot\tau_{s/c}^3\cdot 10^3}$;

$$B = \frac{-3a\cdot\tau_{s/c.}^3\cdot 10^3}{8\cdot\pi\cdot\gamma};$$

$\tau_{s/c}$ is the residence time of the droplet at the end of the electrode, s;

a is a coefficient of 0.33×10^{-4} g/s³;
π is a mathematical constant equal to the ratio of the circumference to the length of the diameter, irrational number ≈ 3.14;
γ is the density of liquid metal, g/mm³;
R is the radius of surface curvature of the droplet, mm;
r_0 is the radius of the electrode rod, mm.

Formula (4) demonstrates that the smaller the short circuit, the smaller the radius of the drop of transferred electrode metal. This is consistent with the data from [53], where the droplet diameter can be assessed according to the formula $Dk = 0.2\ \tau_{s/c}$.

The volume of a droplet shaped like a spherical segment with a base equal to the cross-section of the electrode can be calculated using the formula from [52]:

$$V = \left[2R^3 + (2R^2 + r_0^2)\sqrt{R^2 - r_0^2}\right] \cdot 10^{-3},\ \text{mm}^3. \quad (5)$$

The area of the active surface of the interaction droplet can be found by the formula [53]:

$$S = 2\pi R((R - \sqrt{R^2 - r_0^2}) + r_0),\ \text{mm}^2. \quad (6)$$

The calculation of the energy that various power sources put into a drop of electrode metal can be carried out using oscillograms of current and voltage in the arc gap [54]. According to the values of current and voltage at the key points, the research analyzed the thermal effect of welding current on a drop of electrode metal during welding with various types of power sources [55,56], and the Joule law was applied to calculate the heat introduced into the drop, taking into account the energy passing into the drop [26]:

$$Q = 0.24 \cdot I \cdot U \cdot t,\ J, \quad (7)$$

where I is the strength of the welding current, A; U is the voltage, V; t is the welding time, s.

Using the oscillogram data, the calculation of the heat introduced can be carried out using two methods [55]: grapho-analytic and analytical.

The grapho-analytic method uses discrete oscillogram values as initial data for calculation according to the following equation:

$$Q = 0.24 \cdot \sum_{n=1}^{m} I \cdot U \cdot t,\ J, \quad (8)$$

where n, m is the number of instantaneous of measured values on the oscillogram (Figure 4), I is the welding current strength, A; U is the voltage, V; t is the welding time, s.

To solve the problem using this method, a variety of current and voltage values must be used over time.

The analytical method takes into account errors in the experimental equipment and the sawtooth curve that reflects the welding current during the formation and transfer of the droplet to the weld pool. Changes in current and voltage can be accurately represented as straight line segments synchronized in time. The energy spent on melting electrode metal per unit of time can be calculated using the following equation:

$$Q(t) = 0.24 \sum_{i=0}^{i=n} \int_{t_n}^{t_{n+1}} I_n(t) \cdot U_n(t) \cdot t \cdot dt,\ J. \quad (9)$$

The methodology [55] was adapted to MMAW using the MatLab 2014 software package. It was used as an algorithm for calculating the heat content of a drop during welding with various types of power supply [56]:

$$u_1 = [u_1;\ u_2;\ u_3;\ u_4;\ u_5;\ u_6;\ \ldots];$$
$$i_1 = [i_1;\ i_2;\ i_3;\ i_4;\ \ldots];$$
$$[U_1,\ I_1] = \text{meshgrid}\ (u_1,\ i_1);$$
$$t_1 = t_1;\ t_2;\ t_3;\ t_4;\ \ldots;$$
$$\text{Qк} = \text{sum}(\text{trapz}(0.2 \ldots 0.3 \cdot U_1 \cdot I_1 \cdot t_1)),$$

where u_1, u_2 … u_n are the instantaneous values of voltage, V; i_1, i_2, … i_n are currents, A; and t_1, t_2, … t_n are units of time, s.

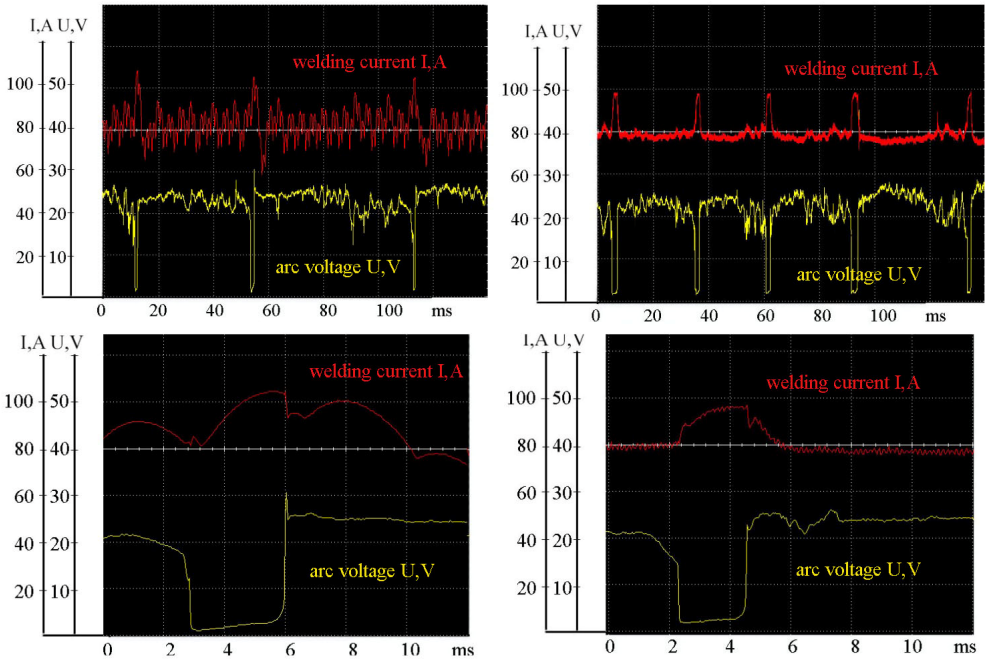

Figure 4. Oscillograms of current in the welding circuit and arc voltage between electrode and workpiece: (LB-52U electrodes of 3.2 mm diameter): (**a**) diode rectifier; (**b**) inverter rectifier.

The heat input into an electrode metal droplet can be estimated by calculating the temperature of the droplets overheating when they pass through an arc gap with short circuits, according to the formula [51]:

$$\Delta T_k = \frac{1}{c}\left(\frac{q_1}{a \cdot \tau_{s/c}^2} - \frac{1}{K}\right), \quad (10)$$

where ΔT_k is the excess of the average temperature of the liquid metal at the electrode above the melting point, °C; c is the average heat capacity of the liquid metal, J/ g °C, c = 0.84 J/ g °C; q_1 is the thermal power of the arc at the end of the electrode, J/s; K is the coefficient characterizing the mass of the metal, which can be melted with a single energy, g/J, $K = 1.5 \times 10^{-3}$ g/J; $\tau_{s/c}$. is the residence time of the droplet at the end of the electrode, s; a is a coefficient 0.33×10^{-1} g/s^3 [4].

Experimental studies were conducted to investigate the effect of the rate of change of the main energy parameters of one welding mode microcycle of the selected power source on the stability of the welding process (Table 1).

Table 1. Parameters of surfacing modes for various brands of electrodes and power supplies.

Type of Power Supply: Rectifier	Brand of Electrodes	Average Values of Mode Parameters (Oscilloscope AKIP-4122/1 V (AKIP, China))	Number of Short Circuits during Cladding Time
diode	LB-52U	Current: 83 + 2.7 A Voltage: 20.8 + 0.6 V Projected welding speed: 0.25 m/min	17
inverter			22
diode	UONI13/55	Current: 83 + 2.7 A Voltage: 21.5 + 0.6 V Projected welding speed: 0.29 m/min	17
inverter			22
diode	CL11	Current: 84 + 2.7 A Voltage: 24.5 + 0.6 V Projected welding speed: 0.27 m/min	12
inverter			24

The analysis of the obtained results (Table 1) shows an increase in the number of short circuits of the arc gap at the same value of the welding mode parameters, which indicates the advantages of the inverter rectifier over the diode rectifier. The advantage is expressed in the reduction of the period between short circuits, which may indicate the transfer of electrode metal in smaller droplets.

Different patterns of current change in the welding circuit and arc voltage between the electrode and the workpiece, shown in Figures 4 and 5, can be explained from the point of view of higher-quality indicators of rectified voltage. The conversion frequency of the inverter power source can reach up to 200 kHz, while that of the diode rectifier can reach up to 300 Hz. This parameter affects the voltage ripple factor of the rectifier, reaching 25% in inverters and 65% in diodes [2,3,55]. Given the above considerations, it can be reasonably concluded that at a thermal time constant of 10^{-5}–10^{-3} s in a shorter interval of current failure, the interelectrode gap lacks the requisite time to cool down and deionize significantly. Consequently, the use of electrodes with fewer ionizing elements in the coating when welding from an inverter rectifier is more reasonable due to a more stable process of arc burning.

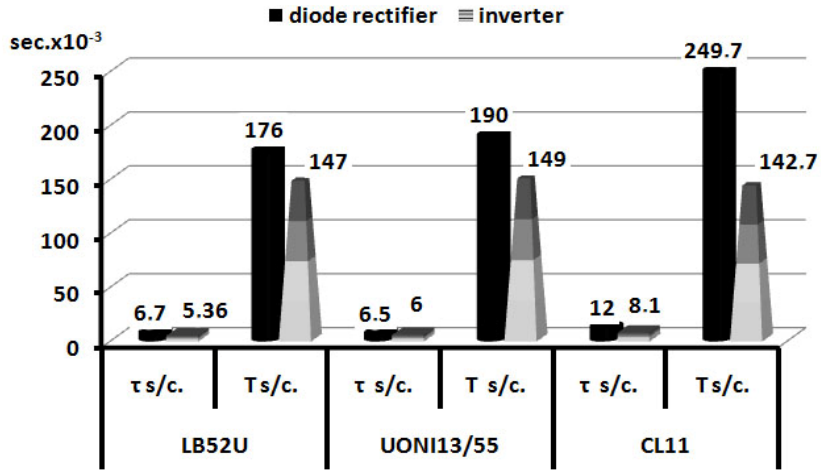

Figure 5. Histograms of the dependence of the averaged arc gap short circuit time $\tau_{s/c}$ and the time of the full cycle of drop formation and transfer $T_{s/c}$ on the type of power source.

Works [2,54,57–62] established that the reduction of the size of the transferred droplets of the molten electrode metal contributes to the defect-free welds and to the increase of the impact strength of the seam metal at low temperatures. We analyzed and statistically processed the oscillograms of current and voltage in the welding circuit (Figure 4) when using power sources with different forms of energy conversion. The results obtained are presented in Table 2 and Figure 5.

Table 2. Results of static processing of electrode metal droplet transfer parameters.

Parameters	Type of Power Supply: Rectifier	Brand of Electrode		
		LB-52U	UONI13/55	CL11
Short-circuit duration of the arc interval $\tau_{s/c}$, μs	Diode	6.7	6.5	12
	Inverter	5.36	6	8.1
RMS deviation of short-circuit duration, $\sigma\tau_{s/c}$, ms	Diode	1.85	2.1	3.8
	Inverter	1.34	1.9	2.3
Coefficient of short-circuit duration variation, $KV\tau_{s/c}$, %	Diode	27.6	32.3	28
	Inverter	25	31.9	28.7
Cycle duration, $T_{s/c}$, ms	Diode	179	190	249.7
	Inverter	147	149	142.7
RMS deviation of cycle duration σ $T_{s/c}$., ms	Diode	52	52	58.7
	Inverter	15	27	29.3
Coefficient of cycle duration variation $KV_{Ts/c}$., %	Diode	29	27.2	23
	Inverter	10	27.48	20

The analysis of the results shown in Table 2 and Figure 5 showed a and ($\tau_{s/c}$ and $T_{s/c}$) an increase in the number of short circuits (Table 1) when using an inverter rectifier; thus, there is a finer drop transfer of electrode metal [5,7]. The obtained regularity can be explained by the difference in oscillograms of welding processes (Figure 4); the experimental setup and the technique of obtaining oscillograms are described in [63]. Power sources with different forms of energy conversion were analyzed taking into account the amplitude values of drop transfer mode parameters (Figure 6). The obtained results are presented in Tables 3 and 4.

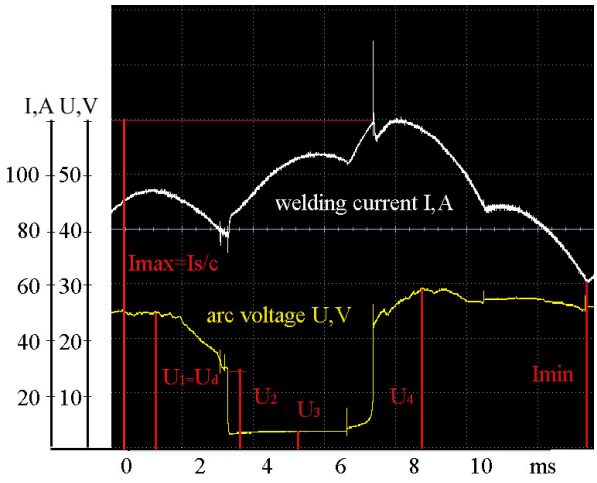

Figure 6. Scheme for determining the amplitude values of welding mode parameters: U_1 is arc voltage, U_2 is arc voltage at the time of touching the drop in the weld pool, U_3 is arc voltage during the transition of the drop from the electrode surface to the weld pool and arc voltage after the transition and at the beginning of the formation of a new drop. Imax is the maximum current during the transition of the drop from the electrode surface to the weld pool (I); *Imin* is the minimum current after the transition of the drop from the electrode surface to the weld pool.

Table 3. Results of statistically processed current oscillograms in the welding circuit and voltage between the electrode and the workpiece (Figures 4 and 5).

Parameters	Type of Source: Rectifier	Brand of Electrode		
		LB-52U	UONI13/55	CL11
Imax, A	Diode	109.9 + 3.3	115.5 + 2.7	118.1 + 3.7
	Inverter	100.2 + 0.8	104.2 + 0.6	102 + 1.6
Imin, A	Diode	61.3 + 3.4	63.1 + 2.1	65.9 + 4.8
	Inverter	73.1 + 0.8	79.3 + 0.8	78 + 1.1
$\frac{I_d}{I_{mx}} \rightarrow 1$,	Diode	0.75	0.73	0.71
	Inverter	0.83	0.8	0.82
V of Imax rise, kA/s	Diode	7.3 + 2.6	8.1 + 0.8	8.3 + 0.3
	Inverter	15.5 + 1.6	15.5 + 1.5	11.2 + 0.3
V of Imin fall, kA/s	Diode	10.3 + 2.2	12.3 + 2.2	11.2 + 0.8
	Inverter	18 + 1.1	18 + 1.1	19 + 1.9

Table 4. Parameters of the arc voltage between the electrode and the workpiece (Figure 5).

Brand of Electrode	Power Source							
	Diode Rectifier				Inverter Rectifier			
	U_1, V	U_2, V	U_3, V	U_4, V	U_1, V	U_2, V	U_3, V	U_4, V
LB-52U	16.9 ± 2.5	14.1 ± 0.9	1.1 ± 0.2	40.9 ± 5.8	18.4 ± 2.7	15.1 ± 1.1	0.7 ± 0.2	26.5 ± 5.7
UONI 13/55	20.4 ± 2	15.76 ± 2.4	0.7 ± 0.1	39.3 ± 5.1	19.9 ± 2.8	15.4 ± 1.4	0.7 ± 0.2	24.4 ± 2.3
CL11	23.4 ± 4.3	21.7 ± 2.4	3.5 ± 0.3	40.6 ± 4.9	23.7 ± 3.5	19.7 ± 1.4	3 ± 0.2	25.2 ± 2.5

The analysis of the results (Tables 2 and 3) confirms the change of mass transfer properties, including the frequency and size of the transferred electrode metal droplets, by reducing the arc burning duration, stabilizing the short-circuit current amplitude, and increasing the short-circuit current rise and fall rates.

The analysis of the results shown in Table 4 showed an increase in the arc voltage jump between the electrode and the workpiece after the short circuit (U4, Figure 6) up to 40% when using a diode rectifier, which can be explained by the inductance of the conversion system (accumulation of excess energy at the moment of the short circuit) realized in this type of power supply.

Application of inverter power sources for manual arc welding with coated electrodes with a higher rate of change of the main energy parameters within one mode microcycle (on average doubled) in comparison with diode rectifiers provides increased stability of the welding process and efficiency of heat and mass transfer, including:

- reduction of the volume of transferred droplets of molten electrode metal to the weld pool by 24% on average, which increases the transfer of chemical elements from the electrode to the weld metal;
- reduction of the average duration of arc burning in the intervals of electrode melting and formation of electrode metal droplets by 36% on average, which contributes to the reduction of overheating of the welded product.

This study examined the impact of the rate of change in the primary energy parameters of one microcycle within the welding mode of the power source on the parameters of the transferred electrode droplets. Taking into account the parameters of the transfer of

electrode metal droplets (Table 2), we calculated the geometric dimensions of the transferred electrode metal droplets (Table 5, Figure 7).

Table 5. Average statistical calculated data of mass and radius of carried electrode metal droplets.

Type of Power Supply: Rectifier	Brand of Electrode	$\tau_{s/c}$, 10^{-3} s	Droplet Weight, mg	Droplet Radius, mm	Droplet Volume, mm^3
Diode	LB-52U	6.7 ± 1.85	0.099 ± 0.002	1.39 ± 0.026	6.89 ± 1.9
Inverter		5.36 ± 1.34	0.052 ± 0.015	1.05 ± 0.01	4.36 ± 1.38
Diode	UONI13/55	6.5 ± 2.1	0.091 ± 0.004	1.3 ± 0.03	6.5 ± 1.99
Inverter		6 ± 1.9	0.071 ± 0.002	1.23 ± 0.02	5.66 ± 1.8
Diode	CL11	12 ± 3.8	0.57 ± 0.04	2.5 ± 0.05	15.48 ± 4.9
Inverter		8.1 ± 2.3	0.175 ± 0.05	1.8 ± 0.04	10.28 ± 2.9

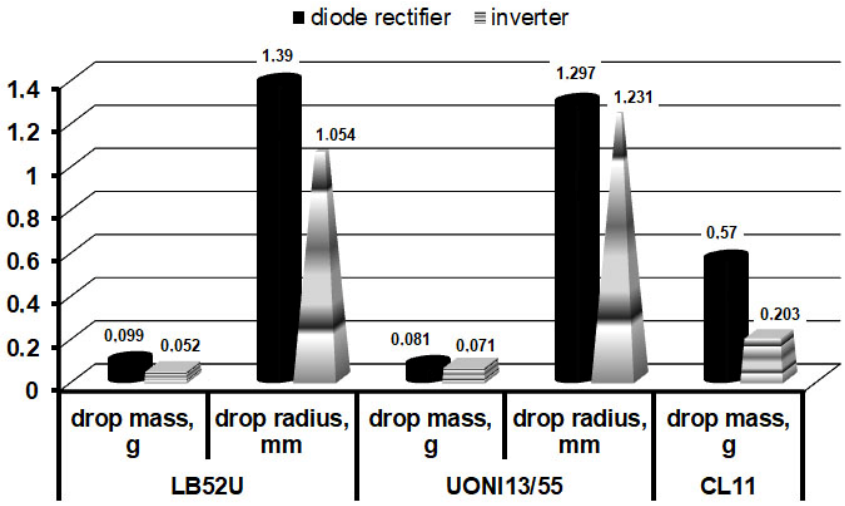

Figure 7. Diagrams of dependence of mass and size of carried electrode metal droplets on the type of power source and brand of coated electrode.

The analysis of the data in Table 5 and Figure 7 revealed that the use of the inverter rectifier allows for a reduction in the volume of the transferred drop of electrode metal up to 37%, which provides a more stable transfer of fine drops.

Experimental studies with high-speed motion pictures were carried out to confirm the adequacy of the obtained results of the theoretical calculation presented in Table 5. The high-speed movie images were processed by the simulation and visualization method [63] (Figure 8), which confirmed the obtained calculation data presented in Table 2.

We have studied the changes in the heat content of the transferred electrode droplets and the pattern of temperature field distribution on the surface of the welded product as a function of the rate of change of the main energy parameters within one welding mode microcycle of the power source. Existing changes in the heat content of electrode metal droplets when using power sources with different dynamic properties have an impact on the distribution of thermal fields in the welded product.

Using the parameters of electrode metal droplet transfer (Table 2) and the previously developed software [64], we were able to estimate the overheating temperature of electrode droplets at MMAW (Table 6).

The analytical calculations [55,56] show that at welding with an inverter rectifier, the average energy spent on melting electrode metal for 1 s is Qk = 1.13 × 10^7 J (Qk = 0.13 × 10^7 J per drop), and at welding with a diode rectifier, Qk = 1.25 × 10^7 J (Qk = 0.156 × 10^7 J per drop).

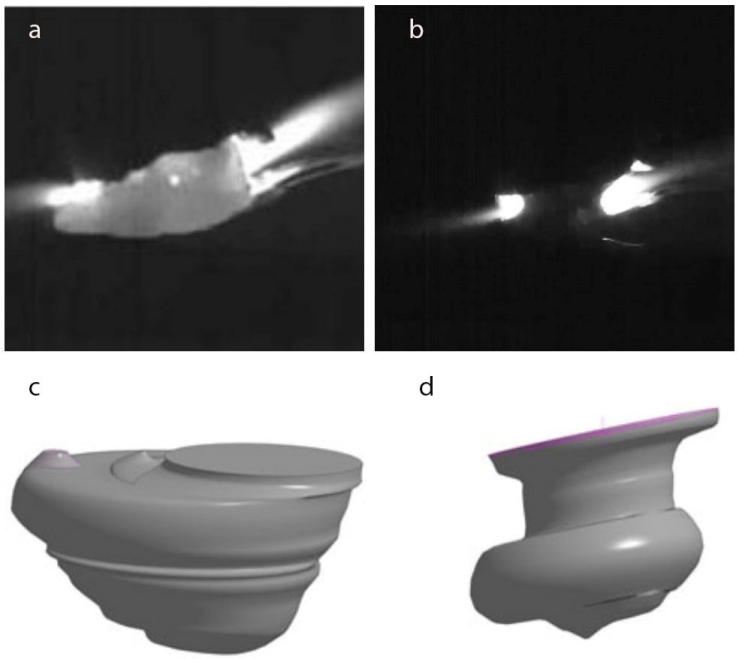

Figure 8. Kinograms of the process of transferring drops of electrode metal during RDS ((**a**): diode, (**b**): inverter), Solid State Modeling of the Spatial Shape of a Drop ((c): diode, (**d**): inverter).

Table 6. Overheating temperature of electrode metal droplets.

Type of power Supply: Rectifier	Brand of Electrodes	$\tau_{s/c}$., 10^{-3} s	$\Delta T_{s/c}$ Average, °C
Diode	LB-52U	6.7 ± 1.85	694
Inverter		5.36 ± 1.34	1496
Diode	UONI13/55	6.5 ± 2.1	888
Inverter		6 ± 1.9	1061
Diode	CL11	12 ± 3.8	30
Inverter		8.1 ± 2.3	130

The different heat content of electrode metal droplets (Table 6) and the time a droplet remains on the electrode surface (Table 2) cause a change in the size of the transferred droplets. Droplets of different sizes have various active surfaces interacting with the slag and the atmosphere and, accordingly, the effectiveness of the metallurgical reactions [21].

The research methodology [55,65–69] was chosen to obtain a real picture of the temperature field distribution, taking into account the dynamic properties of power sources, melting kinetics, and the transfer of electrode metal. In the course of the study, the manual arc cladding of a roll with coated electrodes of the LB 52U brand was carried out on a 100 × 150 mm plate with a thickness of 6 mm made of 09G2S steel. The power source used was an inverter rectifier and a diode rectifier. The fields were imaged with a FLIR ThermaCAM P65HS (FLIR Systems, Täby, Sweden) thermal imager at a frequency of 1 frame per second and a temperature sensitivity of 0.05 °C [66–68]. The imaging was performed (Figure 9) during the welding time of one pass at a speed of 5 fps. The adequacy of the obtained results of temperature fields was checked with the help of a C-500 infrared pyrometer.

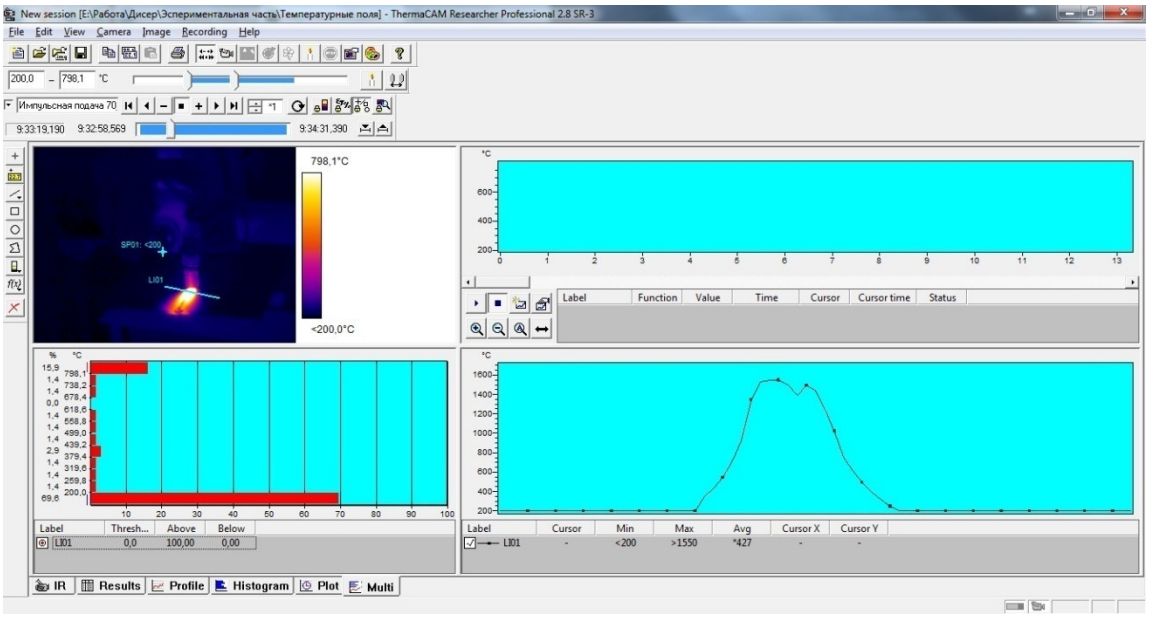

Figure 9. Example of recording temperature fields in the working window of ThermaCAM Researcher (FLIR Systems, Täby, Sweden) program.

The obtained thermograms (Figure 10) give a clear picture of the changes in the temperature fields of the welded product. However, it is difficult to determine the coordinates of the points corresponding to a particular isotherm from the obtained images. This is due to the fact that the thermal imaging of the welding process was performed at an angle to the welding axis and at an angle to the plane of the welded plates.

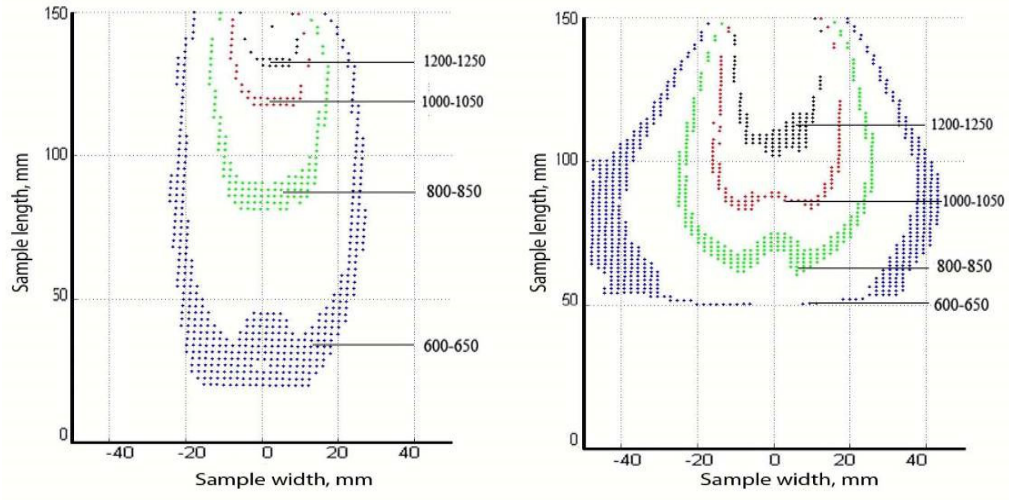

Figure 10. Patterns of temperature fields on the surface of the product welded by MMAW (electrodes LB-52U, diameter 3.2 mm), mode parameters Iw = 100 + 3A, Uw = 22 + 0.6 V, Vw = 13. . .14 cm/min: (**a**). inverter rectifier; (**b**). diode rectifier.

In order to obtain a frontal image of the temperature fields suitable for further study, the obtained data were processed using the ThermaCAM Researcher application and the MATLAB program package [66].

The differences in the patterns of thermal field distribution on the plate surface during cladding by power sources with different dynamic properties (Figure 10) confirm the presence of changes in the heat content of the weld pool melt during the cladding process [69].

Due to the decrease in the residence time of the molten metal droplets at the electrode end and the corresponding increase in the frequency of their transfer (Figures 6 and 8), in the case of cladding from the inverter rectifier, there is a noticeable increase in the length of the temperature field isotherms and a significant decrease in their width, which confirms the increase in the crystallization rate of the weld pool in this case. This, in turn, is associated with a decrease in the heat content of the electrode metal droplets (Table 6).

The obtained results agree with the data obtained in [2,28,62,67,68], where it is proven that the smaller the size of the transferred droplets and the higher the frequency of their transfer, the lower the heat content of the weld pool. Therefore, the temperature field in the case of inverter rectifier application is narrower (by about 25%), which should be accompanied by a higher rate of melt crystallization and, consequently, less influence on the thermo-deformation changes in the zone of permanent joint. The latter circumstance will be crucial for the reduction of residual stresses and will significantly limit the growth of structural components in the zone of the permanent joint.

We have carried out studies on the influence of the rate of change of the main energy parameters of one welding mode microcycle of the power source and the chemical composition of the welded electrode metal (Tables 7–10).

A technique for obtaining clad samples was developed [70] to evaluate the effect of the dynamic properties of power sources and different methods of energy conversion on the transition of chemical elements from the coated electrodes to the weld seam and slag crust. The technique permits the chemical composition of the electrode metal to be determined by cladding a roll on a copper plate, with the insertion of a metal electrode rod of the same brand, cleaned from the flux, into the groove of the plate. The inserted electrode rod is the substrate for the cladding. This ensures the homogeneity of the electrode-clad metal and reduces the time spent obtaining the samples to be studied.

The analysis of the thermodynamic properties of alloying elements included in the chemical composition of the electrode metal rod (Table 7) determined that the elements Mn and Si are most sensitive to changes in the heat content of electrode metal droplets. The thermophysical properties of these elements (Table 8) are associated with their rate of burning out: the lower the burning temperature, the faster the burning out process.

Table 7. Empirically obtained chemical composition of the electrode rod.

Brand of Electrode	Elements Content, wt. %						
	C	Si	Mn	S	P	Cr	Ni
CL11	0.05–0.09	less than 0.70	1.50–2.00	less than 0.018	less than 0.025	18.50–20.50	9.00–10.50
LB-52U	0.11	0.2	0.41	0.010	0.021	0.04	0.02
UONI13/55	0.07	0.4	0.38	0.020	0.020	0.02	0.03

Table 8. Thermodynamic properties of simple substances (under normal conditions) are included in the chemical composition of the metal electrode rod [71].

Name	Substance				
	Mn	Si	Cr	Ni	C Graphite
Melting point, K	1517	1688	2130	1726	3820
Boiling point, K	2235	2623	2945	3005	5100
Heat of vaporization, kJ/mol	221	383	342	378.6	-
Density, g/cm^3	7.21	2.33	7.19	8.9	2.25

Table 9. Chemical composition of the welded electrode metal (main chemical elements for the study).

Electrode, Type of Power Supply: Rectifier	Si, %	Mn, %	Cr, %	Ni, %
CL11, diode	0.29 ± 0.02	2.44 ± 0.08	11.43 ± 0.19	8.10 ± 0.16
CL11, inverter	0.39 ± 0.02	2.48 ± 0.08	11.85 ± 0.19	8.59 ± 0.16
LB 52U, diode	0.17 ± 0.02	0.72 ± 0.03	0.05 ± 0.01	0.05 ± 0.08
LB 52U, inverter	0.33 ± 0.02	1.00 ± 0.05	0.08 ± 0.01	0.06 ± 0.08
UONI 13/55, diode	0.25 ± 0.02	0.94 ± 0.05	0.05 ± 0.01	0.06 ± 0.08
UONI 13/55, inverter	0.33 ± 0.02	1.10 ± 0.05	0.10 ± 0.01	0.06 ± 0.08

Table 10. Chemical composition of slug.

Electrodes	Type of Power Supply: Rectifier	CaO, %	SiO_2, %	TiO_2, %	NbO, %	MnO, %	Fe_2O_3, %	Cr_2O_3, %	Al_20_3, %
CL11	diode	62.33	12.48	7.27	6.31	3.53	3.52	3.29	1.27
	inverter	60.64	12.14	6.31	5.67	3.48	8.26	2.74	0.76
LB-52U	diode	38.66	25.37	9.57	0.05	7.48	15.09	0.17	3.61
	inverter	36.27	24.18	8.74	0.10	7.21	19.69	0.15	3.66
UONI 13/55	diode	50.95	24.18	3.95	0.02	5.80	7.53	-	7.57
	inverter	47.44	23.65	3.84	0.02	4.93	12.96	-	7.16

The results of the analysis of the obtained data of the chemical composition of the welded metal and slag (Tables 9 and 10), when using the inverter rectifier in comparison with the diode rectifier, show that.

1. Increase in the mass percentage of alloying elements in the weld metal:
   - Si from 0.29% to 0.39% using CL11, from 0.17% to 0.33% using LB-52U, and from 0.25% to 0.33% using UONI13/55;
   - Mn from 2.44% to 2.48% using CL11, from 0.72% to 1.00% using LB-52U, and from 0.94% to 1.1% using UONI13/55;
   - Cr from 11.43% to 11.85% using CL11, from 0.05% to 0.08% using LB-52U, and from 0.05% to 0.1% using UONI13/55.
2. Decrease in the percentage of oxides 5% (SiO_2, MnO) in the slag phase.

The obtained results can be explained by the decrease in the size of the transferred molten metal droplets and their lower heat content when the welding arc is supplied by the inverter rectifier, which has high rates of change in the main energy parameters of one welding mode microcycle.

The analysis of the chemical composition of the weld metal has shown (Tables 11–14) that the type of power source affects the chemical composition of the weld, which is also confirmed by the authors of [72–79]. The dynamic properties of the inverter rectifier provide a higher rate of welding current rise, which in turn limits the short-circuit current [2,3] and provides a fine drop transfer of electrode metal (Table 5).

Table 11. Chemical composition of metal for welds on Ø159×6 pipe (09G2S steel) with LB-52U electrodes.

Power Source: Rectifier	Elements Content, wt. %							
	C	Si	Mn	S	P	Cr	Ni	Cu
diode	0.10 ± 0.012	0.52 ± 0.03	1.03 ± 0.05	0.010 ± 0.002	0.014 ± 0.003	0.03 ± 0.01	0.05 ± 0.01	0.03 ± 0.008
inverter	0.09 ± 0.005	0.60 ± 0.03	1.23 ± 0.05	0.010 ± 0.002	0.014 ± 0.003	0.03 ± 0.01	0.06 ± 0.01	0.03 ± 0.008

Table 12. Chemical composition of metal for welds made on steel 45 with UONI13/55 electrodes.

Type of Power Supply: Rectifier	Elements Content, wt. %						
	C	Si	Mn	P	Cr	Ni	Cu
diode	0.11 ± 0.012	0.30 ± 0.02	0.92 ± 0.05	0.019 ± 0.003	0.06 ± 0.01	0.05 ± 0.01	0.09 ± 0.012
inverter	0.12 ± 0.012	0.31 ± 0.02	1.00 ± 0.05	0.02 ± 0.003	0.06 ± 0.01	0.06 ± 0.01	0.10 ± 0.012

Table 13. Chemical composition of metal in welds made of 12H18N10T steel with CL11 electrodes.

Power Source: Rectifier	Elements Content, wt. %							
	C	Si	Mn	S	P	Cr	Ni	Nb
diode	0.12 ± 0.012	0.80 ± 0.03	1.04 ± 0.05	0.008 ± 0.002	0.018 ± 0.003	18.08 ± 0.2	9.23 ± 0.16	0.70 ± 0.08
inverter	0.12 ± 0.012	0.82 ± 0.03	1.23 ± 0.05	0.008 ± 0.002	0.018 ± 0.003	18.45 ± 0.2	10.01 ± 0.16	0.70 ± 0.08

Table 14. Chemical composition of the welded samples base metal.

Steel	Elements Content, wt. %							
	C	Si	Mn	S	P	Cr	Ni	Cu
45	0.42–0.5	0.17–0.37	0.5–0.8	<0.035	<0.03	<0.25	<0.30	<0.30
09G2S	<0.12	0.5–0.8	13–1.7	<0.035	<0.03	<0.25	<0.30	<0.30
12H18N10T	<0.12	<0.8	<2	<0.035	<0.02	17–19	9–11	<0.30

Macro and microstructural studies of welded specimens were carried out by optical metallography on cross sections according to the scheme shown in Figure 11. An Olympus GX-71 optical microscope (Olympus, Tokyo, Japan) was used. The manufacture of sections employed mechanical grinding, mechanical polishing on diamond paste ACM 10/7 NVL, and chemical etching in a four-percent alcohol solution of nitric acid.

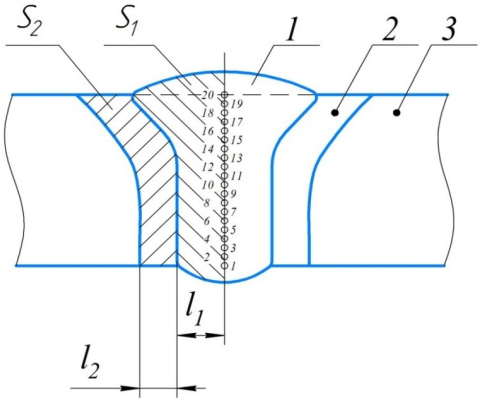

Figure 11. Scheme of measurements (step between points is 0.5 mm): 1 is welded seam; 2 is HAZ; 3 is base metal; l_1 is the length of the weld; l_2 is the width of HAZ; S_1 is the area of the weld; S_2 is the area of HAZ.

Macro-sections processed according to the scheme shown in Figure 11 are presented in Figure 12, and the measured values are in Table 15.

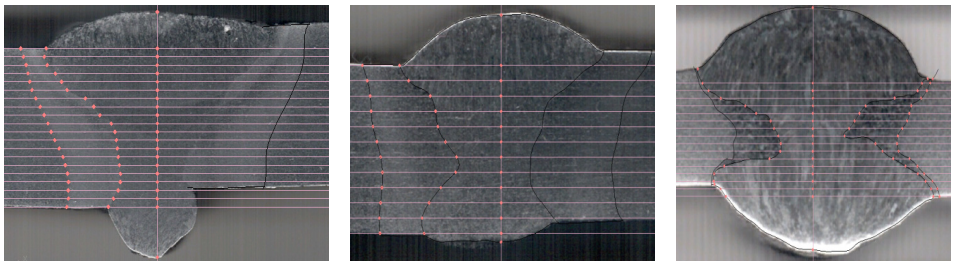

(**a**) (**b**) (**c**)

Figure 12. Scheme of macro-sections processing in Compass-3D v21 software: (**a**) is steel 09G2S, (**b**) is steel 45, (**c**) is steel 12H18N10T.

Table 15. Experimental data of macro-sections processing.

Steel	Type of Joint According to GOST	Type of Power Supply: Rectifier	Area of Welded Metal, mm^2	Width of Welded Metal, mm	HAZ Area, mm^2	HAZ Width, mm
45	C17 thickness 10 mm	Diode	133 ± 5.1	4.06 ± 0.04	95.5 ± 2.9	5.17 ± 0.04
		Inverter	129 ± 2.6	4 ± 0.04	80.6 ± 2.8	3.34 ± 0.03
09G2S	C17 thickness 6 mm	Diode	23.6 ± 0.4	3.33 ± 2.6	51.8 ± 0.53	2.08 ± 0.06
		Inverter	21.4 ± 0.3	2.89 ± 0.94	42.6 ± 0.28	1.58 ± 0.04
12H18N10T	C7 thickness 3 mm	Diode	43.8 ± 0.3	3.73 ± 0.07	10.3 ± 0.7	1.48 ± 0.05
		Inverter	40.1 ± 0.6	3.28 ± 0.05	6 ± 0.47	1.01 ± 0.05

The data analysis (Table 15) revealed the reduction of the HAZ area by 15% and the average width of the HAZ by 36% when using the inverter rectifier in comparison with the diode rectifier. Fractures in welded structures most often occur in the HAZ [79–83], with the extent and properties depending on the welding thermal cycle parameters.

Microstructural studies were carried out on welded joints made of steel 09G2S with electrodes LB-52U (Figures 13 and 14); steel 45 with electrodes UONI 13/55 (Figures 15 and 16); steel 12H18N10T with electrodes CL11 (Figures 17 and 18) to obtain a complete picture of the effect of the change rate of the main energy parameters of one welding mode microcycle of the power source on the operational properties of welded joints.

The clad metal at welding of steel 09G2C by electrodes LB-52U (Figures 13a and 14) with the use of a diode rectifier has an uneven structure of columnar dendrites, which is characteristic of the cast state. The ferritic plates are 1 mm long and 20 μm wide. The space between the plates is occupied by smaller dendrites. At higher magnification, the ferritic plates are found to consist of polyhedral grains of about 14.5 ± 0.28 μm in size. Other phases and structural components, except for ferrite, are not detected, which corresponds to the composition of the LB 52U electrode rod.

The structure of the weld metal in the weld made with the inverter rectifier (Figure 13b) is much more homogeneous. The columnar character is less pronounced. The length of ferrite plates does not exceed 50 μm and the thickness reaches 20 μm. The average size of the ferrite grains forming the dendrites is 12 ± 0.64 μm.

The transition from the clad metal to the HAZ and then to the base metal structure is smooth without abrupt changes for both the diode rectifier (Figure 13c) and the inverter rectifier (Figure 13d). In both cases, the heat-affected zone is represented by polyhedral ferrite grains.

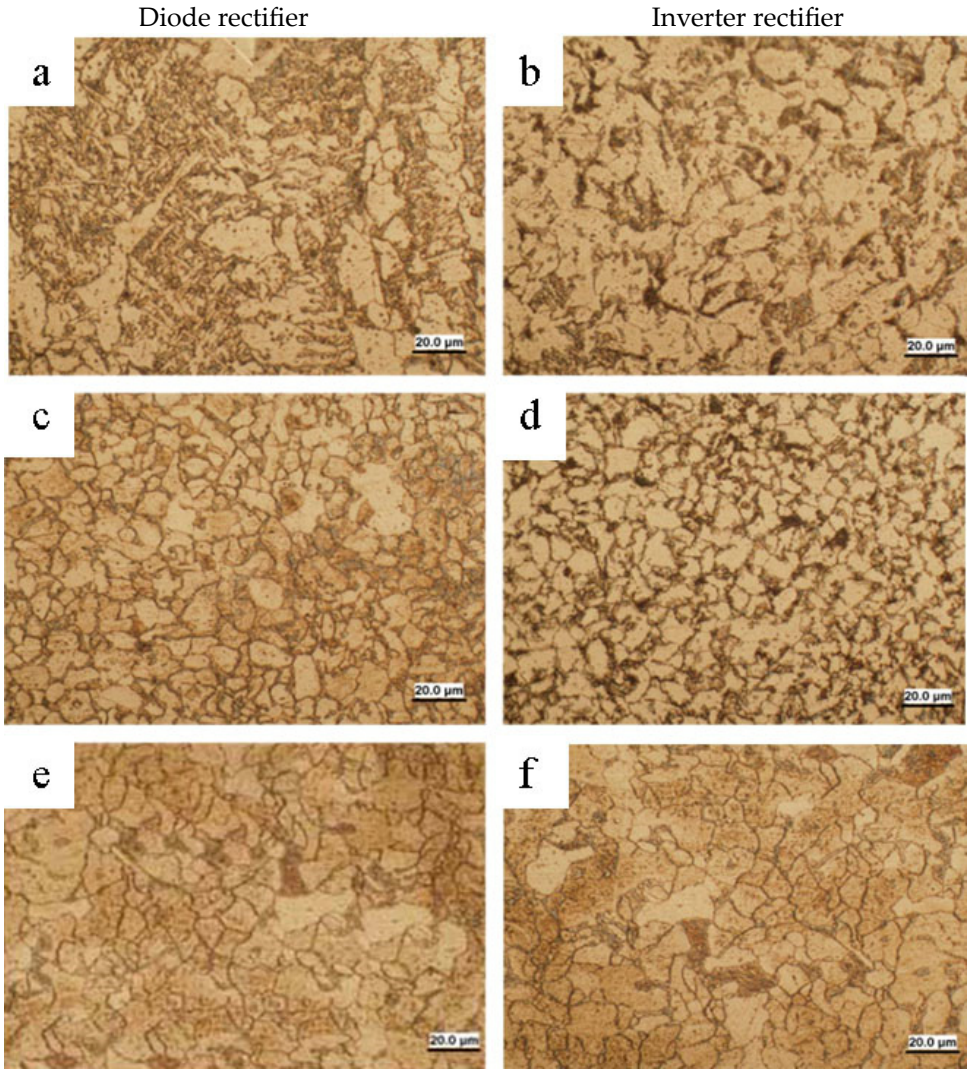

Figure 13. Photographs of the microstructure of 09G2S steel samples: (**a**,**b**) are the weld; (**c**,**d**) are the HAZ; (**e**,**f**) are the base metal.

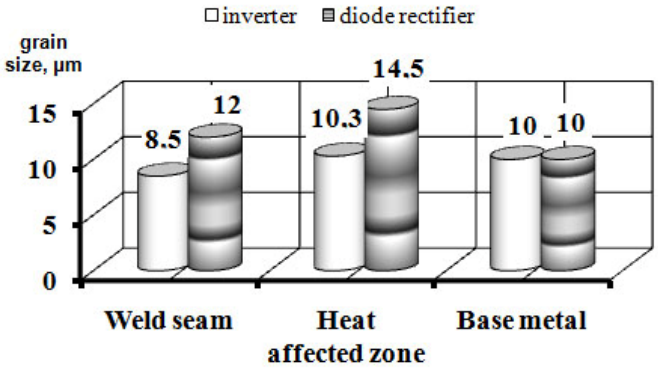

Figure 14. Diagram of ferrite grain size depending on the type of power source.

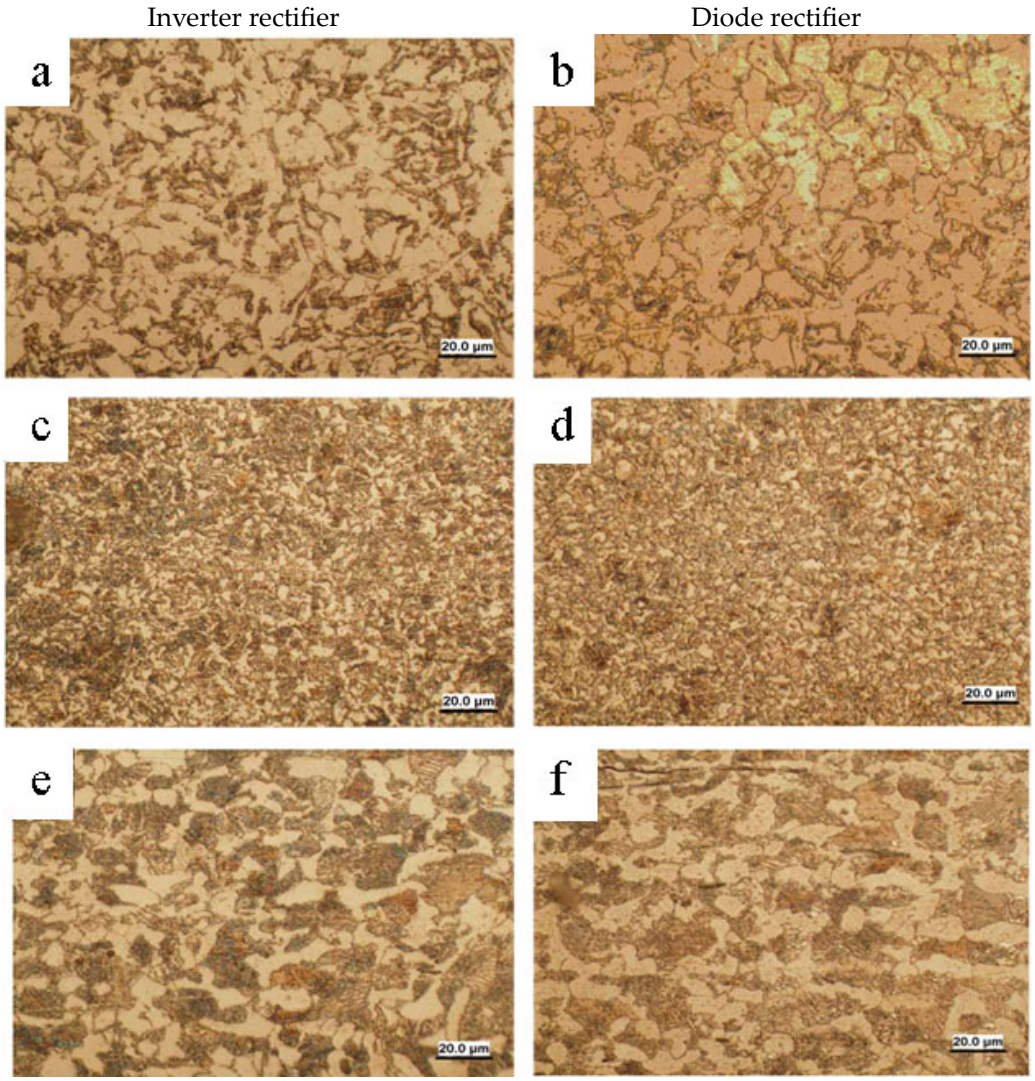

Figure 15. Photographs of the microstructure of steel 45 samples: (**a**,**b**) are the weld; (**c**,**d**) are the HAZ; (**e**,**f**) are the base metal.

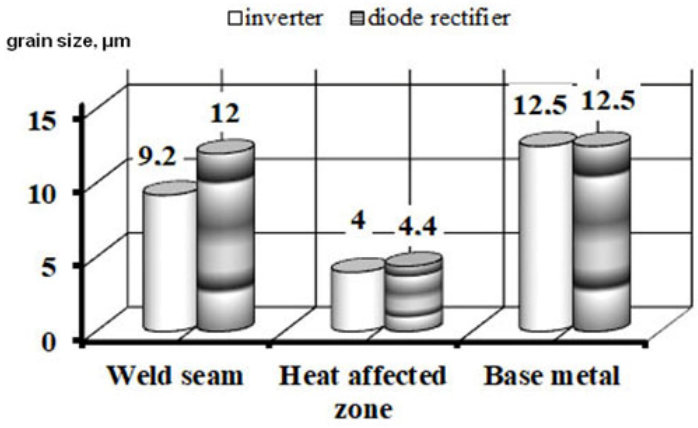

Figure 16. Diagram of ferrite grain size depending on the type of power source.

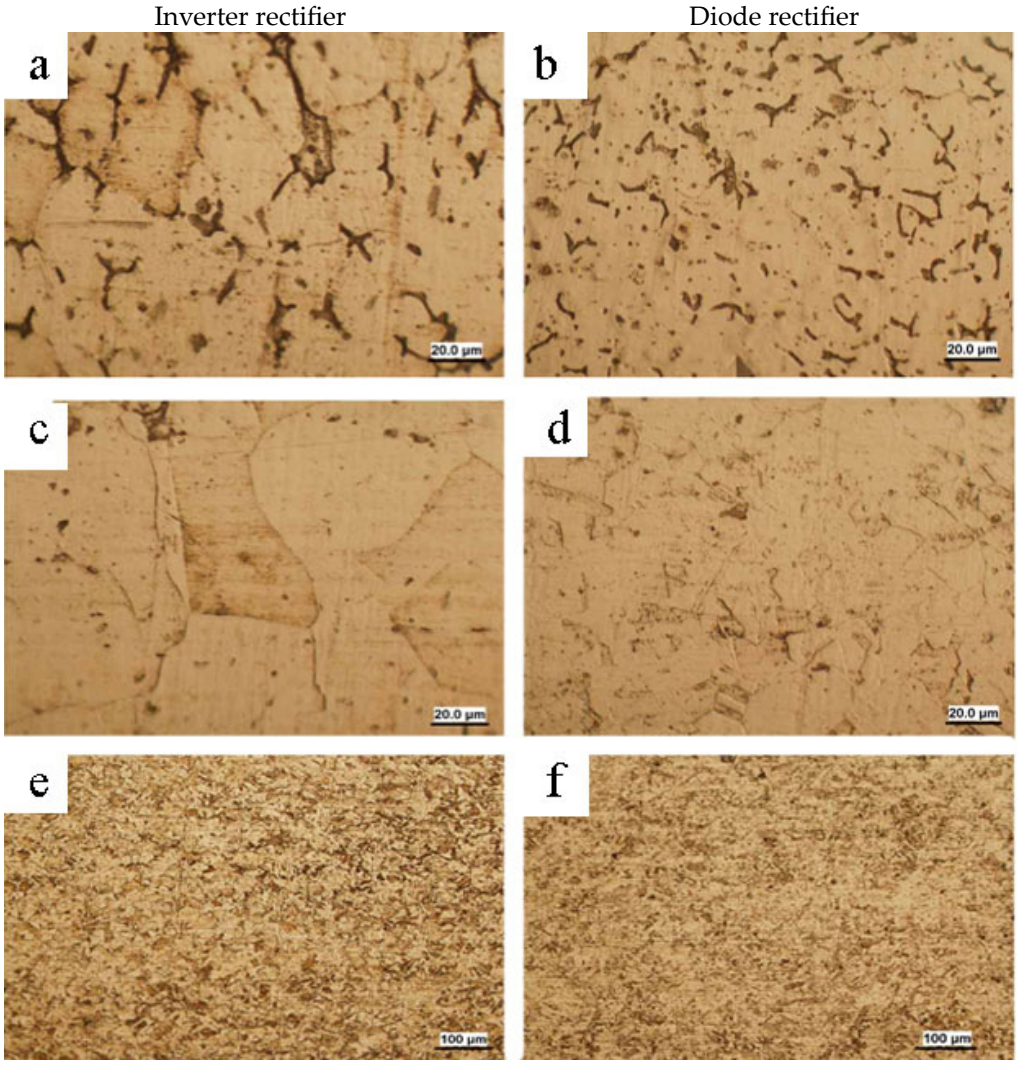

Figure 17. Photographs of the microstructure of 12H18N10T steel samples: (**a**,**b**) are the weld; (**c**,**d**) is the HAZ; (**e**,**f**) is the base metal.

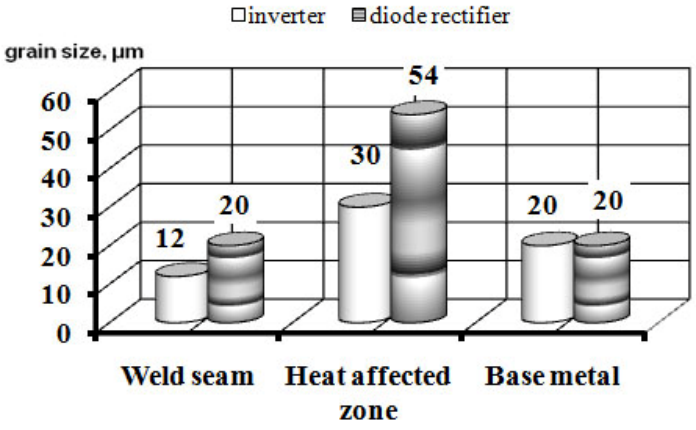

Figure 18. Average grain size in different zones of the weld as a function of the dynamic properties of the power source.

In the heat affected zone of the welded joint obtained using the diode rectifier (Figure 13c), the ferrite grain size is slightly higher and reaches 10.3 ± 0.32 µm. The structure contains pearlite in the amount corresponding to the base metal (09G2S steel). The total width of the HAZ reaches 2 mm, with the inverter rectifier (Figure 13d), and the

average grain size is 8.5 μm. Pearlite inclusions are virtually absent. The width of the HAZ is small and does not exceed 1 mm.

The base metal exhibits a ferrite–pearlite structure (Figure 13e,f). The volume fraction of pearlite is estimated to be 10–12%, which correlates with the chemical composition of 09G2C steel. Ferrite grains are polyhedral with well-defined, clean boundaries.

The structure of the weld metal at welding steel 45 with UONI 13/55 electrodes using inverter source (Figures 15a and 16) is purely ferritic and homogeneous. The average size of ferritic grains is slightly smaller and is ≈9.2 ± 0.54 μm. A small amount of the fine fraction is present.

The welded metal at welding with a diode rectifier is presented in Figure 15b. Ferritic grains are polyhedral and practically equiaxed. The average size of the ferritic grains is ≈12 ± 0.69 μm At high magnification, the gaps between these large grains can be seen, there are conglomerates of very small (less than one micrometer) ferrite grains. Other phases and structural components besides ferrite are not detected, which corresponds to the composition of the UONI13/55 electrode rod (0.07% C).

The transition from the clad metal to the HAZ and then to the base metal structure is smooth without abrupt changes for both the diode rectifier (Figure 16d) and the inverter rectifier (Figure 15c). In both cases, HAZ is a polycrystalline aggregate of ferrite grains and pearlite colonies. The pearlite content increases smoothly with the distance from the clad metal to the base metal, reaching ≈50% by volume.

When a diode source is used (Figure 15d), the average size of the ferrite grains is 4.4 ± 0.67 μm. The same average sizes are also found in the pearlite colonies. The width of the HAZ reaches 8 mm.

In the HAZ of the welded joint obtained using an inverter rectifier (Figure 15c), the ferrite grain size is almost the same, 4 ± 0.32 μm. The total width of the HAZ is significantly smaller (≤6 mm). This indicates less heat input and overheating of the welded product.

The structure of the base metal is ferritic-pearlitic (Figure 15e,f). The volume fraction of pearlite is 55%, which corresponds to the chemical composition of steel 45. The ferrite grains are polyhedral with well-defined boundaries. Their average size is the same in both cases, ≈12.5 ± 0.39 μm.

The structure of the clad metal at welding of steel 12H18N10T with electrodes CL11 using power sources with different dynamic properties is shown in Figure 17a,b. With the use of a diode rectifier in the clad metal, the structure is inhomogeneous, dendrites are of different lengths, well developed, and the width is ≈2 μm. In interdendritic intervals, the metal has a grain structure characteristic of chromium-nickel austenite with a mean size ≈ 20 ± 3.36 μm (Figures 17a and 18). In the case of the inverter rectifier, the clad metal is more homogeneous in structure. The dendrites are on average less elongated, their width is less than 2 μm. The interdendritic space has a larger area. The grain structure is more pronounced, and the average grain size is one and a half times smaller, being ≈12 ± 0.57 μm (Figures 17b and 18).

The HAZ in both cases has a polyhedral grain structure characteristic of chromium-nickel austenite (Figure 17c,d). The average grain size is significantly larger than in the clad metal, especially in the diode source sample, where it reaches 54 ± 3.38 μm (Figure 17c). Some grains contain twins In the HAZ of the inverter rectifier weld, the average grain size is smaller by ≈30 ± 6.28 μm, and the degree of grain twinning is higher (Figure 18d). The HAZ merges smoothly into the base metal without sharp boundaries. The smallest width of the HAZ, 75 μm, was recorded in the joint made by the inverter power supply, and the largest width of 3000 μm was recorded in the joint made by the diode rectifier.

The base metal structure is similar in both samples (Figure 17e,f). The differences in the average size of 20 ± 6.2 μm and 17 ± 3.87 μm are within the statistical error.

The use of an inverter rectifier in MMAW instead of a diode rectifier allows for a welded joint with a more homogeneous and fine-grained structure of welded metal. Differences in the microstructure of the welded joint can be explained by the lower heat

content of the molten electrode metal drop when welding with an inverter rectifier. The reduction of HAZ is provided

We have studied the change in mechanical properties of welded joints made with the use of power sources with different dynamic properties. The results are presented in Tables 16–18.

Table 16. Mechanical properties of welded joints made of Ø159×6 pipe (steel 09G2S) with LB 52U electrodes.

Type of Power Supply: Rectifier	Range of Rupture Strength σB, MPa	Outward, Inward and Rib Bending Angle, deg.	KCU Impact Strength, J/cm^2 (Notch in the Center of the Seam)			
			+20 °C	0 °C	−20 °C	−40 °C
diode	542 + 1	more than 120	197 + 12	219 + 9	226 + 5	182 + 21
inverter	550 + 5	more than 120	219.6 + 3	234.6 + 3	237 + 3	186.8 + 11

Table 17. Mechanical Properties of Welded Joints of 45 Steel Using UONI 13/55 Electrodes.

Power Source	Range of Rupture Strength σ_B, MPa	*KCU* Impact Strength, J/cm^2 (Notch in the Center of the Seam)					
		+20 °C			−40 °C		
		KCU	σ_{KCU}	$K_{V\cdot KCU}$	KCU	σ_{KCU}	$K_{V\cdot KCU}$
diode rectifier	648	96.5	22.15	22	12.58	2.5	19
inverter rectifier	650	121	13.86	11	58.3	8.35	14

Table 18. Mechanical properties of welded joints made of 12H18N10T steel with CL11 electrodes.

Power Source: Rectifier	Range of Rupture Strength σ_B, MPa	Flow Stress σ_T, MPa
diode	589 ± 1	224 ± 26
inverter	593 ± 1	236 ± 36

Data analysis (Table 16) showed an increase in impact toughness for welds made with the inverter rectifier compared to those made with the diode rectifier at different temperatures. This can be explained by the different microstructures in the welds, reduction of ferrite plate length up to 50% in the weld metal, change of HAZ ferrite grain size by 17.5%, and reduction of HAZ length by 25%.

The changes in impact strength shown in Table 17 can be explained by finer droplet transfer when inverter rectifiers are used, as confirmed by [50,84].

The analysis of the data in Table 18 showed insignificant changes in the mechanical properties of the welded joint when welding from different types of power sources. However, the reduction of the HAZ by 50%, which will have a positive effect on the corrosion resistance of the joint, is in favor of the operational reliability of the welded joints obtained with the inverter rectifier [79].

4. Conclusions

1. The use of inverter power sources for manual arc welding with coated electrodes provides increased stability of the welding process as well as heat and mass transfer efficiency in comparison with diode rectifiers:
    - reduction of the volume of droplets transferred to the weld pool by 24% on average, which increases the efficiency of chemical elements transfer from the electrode to the weld metal;

- reduction of the average duration of arc burning in the intervals of electrode melting and formation of electrode metal droplets by 36% on average, which contributes to the reduction of overheating of the welded product;

2. It has been demonstrated that an increase in the rate of change of the main energy parameters of one microcycle of the welding mode (on average doubled) when using an inverter rectifier in comparison with diode rectifiers provides:
   - reduction of the heat content of electrode metal droplets (on average by 15%) contributes to a reduction of the width of temperature fields on the surface of the welded product by 25%, the area of HAZ by 15%, and the width of HAZ by 36%.
   - improved structure of the welded joint by reducing the grain size of the clad metal by 30% on average and the HAZ by 35% on average, as well as the welded joint due to the increased impact toughness by 15%.

Author Contributions: Conceptualization, D.A.C. and D.P.I.; methodology, D.A.C. and D.P.I.; software, D.P.I.; validation, D.A.C., D.P.I., and E.V.L.; formal analysis, D.A.C., D.P.I. and E.V.L.; investigation, D.A.C. and D.P.I.; data curation, D.A.C., D.P.I., and E.V.L.; writing—original draft preparation, D.P.I.; writing—review and editing, D.A.C.; visualization, D.P.I. All authors have read and agreed to the published version of the manuscript.

Funding: The investigation of the grain structures was performed according to the Government research assignment for ISPMS SB RAS, project FWRW-2021-0005.

Data Availability Statement: The raw data supporting the conclusions of this article will be made available by the authors upon request.

Conflicts of Interest: The authors declare no conflicts of interest.

References

1. Vlasov, A.; Makarenko, N.; Holub, D.; Kushchii, H.; Titarenko, V. Increasing of efficiency of manual arc welding and surfacing of engineering products. *Sci. J. Ternopil Natl. Tech. Univ.* **2018**, *91*, 46–55. [CrossRef]
2. Milyutin, V.S. *Testing the Welding Properties of Arc Welding Equipment*; ESAB: Yekaterinburg, Russia, 2019; 466p.
3. Il'yaschenko, D.P.; Chinakhov, D.A.; Gotovshchik, Y.M. MAW Productivity Development and Reduction of its Harmful Effect on Human Organisms. *Appl. Mech. Mater. Sci. J.* **2014**, *682*, 122–126. [CrossRef]
4. Lebedev, V.A.; Sorokin, M.S.; Belov, A.A. Algorithms for controlling inverter sources of welding current to optimize the electrode metal transfer parameters. *Weld. Int.* **2014**, *28*, 957–961. [CrossRef]
5. Słania, J.; Slazak, B. Analysis of the Covered Electrode Welding Process Stability on the Basis of Linear Regression Equation. *Arch. Metall. Mater.* **2014**, *59*, 905–909. [CrossRef]
6. Lebedev, V.A.; Krot, A.F.; Yurashevich, V.G. A method for controlling molten droplet transfer in mechanized welding. *Weld. Int.* **2013**, *27*, 702–704. [CrossRef]
7. Dyurgerov, N.G.; Morozkin, I.S.; Lenivkin, V.A. Integral self-regulation in arc welding processes. *Weld. Int.* **2017**, *31*, 713–716. [CrossRef]
8. Ohara, M.; Mizuguchi, T.; Miyata, K.; Tsuyama, T.; Fujiwara, K. A new approach to controlling metal transfer by dynamic modification in gas composition of arc atmosphere: Studies on pulsed gas MAG welding. *Weld. Int.* **2020**, *34*, 430–454. [CrossRef]
9. Ślązak, B. Analysis of instantaneous values of current and voltage parameters in the evaluation of process stability of shielded electrode welding. *Weld. Int.* **2016**, *30*, 33–37. [CrossRef]
10. Lankin, Y.N. Stability parameters of manual metal arc welding. *Autom. Weld.* **2011**, *1*, 7–15.
11. Skrzyniecki, K.; Kolasa, A.; Cegielski, P. Study of static and dynamic characteristics of welding power source-arc systems. *Weld. Int.* **2015**, *29*, 865–867. [CrossRef]
12. Rykała, J.; Pfeifer, T. Influence of the technological conditions of welding using the MIG/MAG method on metal transfer in the welding arc. *Weld. Int.* **2014**, *28*, 931–940. [CrossRef]
13. Sas, A.V.; Sorokin, V.N.; Chernov, A.V. Ensuring the Stability of Arc Welding Process when Using Inverter Power Sources. *Glob. Nucl. Saf.* **2017**, *22*, 46–53. Available online: https://cyberleninka.ru/article/n/obespechenie-stabilnosti-protsessa-dugovoy-svarki-pri-ispolzovanii-invertornyh-istochnikov-pitaniya (accessed on 21 March 2024). [CrossRef]
14. Yun, D.H.; Lee, W.S.; Lee, J.Y.; Lee, I.O. A 3-leg inverter-based high-frequency welding power supply capable of AC 220 and 440-V operation. *IEEE Trans. Power Electron.* **2021**, *36*, 12877–12888. [CrossRef]
15. Kar, A.; Sengupta, M. Design, analysis and experimental validation of a variable frequency silicon carbide-based resonant-converter for welding applications. *Sādhanā* **2021**, *46*, 75. [CrossRef]

16. Jamrozik, W.; Górka, J. Assessing MMA Welding Process Stability Using Machine Vision-Based Arc Features Tracking System. *Sensors* **2021**, *21*, 84. [CrossRef] [PubMed]
17. Jabavathi, J.D.; Sait, H. Design of a single chip PWM driver circuit for inverter welding power source. *IEEE Trans. Circuits Syst. II Express Briefs* **2019**, *67*, 720–724. [CrossRef]
18. Marneni, A.; Sivani, A.S.; Kumar, S.S.; Babu, N.; Padmanaban, N. Analysis and Control of Energy Efficient Welding Machine Test Bed Employing SiC based Power Electronic Converter. In Proceedings of the 2023 11th National Power Electronics Conference (NPEC), Guwahati, India, 14–16 December 2023; pp. 1–6.
19. Shatilo, S.P. Model of electrode metal transfer at manual arc welding. *Weld. Prod.* **1995**, *9*, 3–5.
20. Qin, R. Critical Assessment of the Electric Effect in Electric Arc Welding. *Metals* **2021**, *11*, 1917. [CrossRef]
21. Novozhilov, N.M. *Fundamentals of Metallurgy of Arc Welding in Gases*; Mashinostroenie: Moscow, Russia, 1979; 231p.
22. Erokhin, A.A. *Fundamentals of Fusion Welding. Physico-Chemical Regularities*; Mashinostroenie: Moscow, Russia, 1973; 448p.
23. Pokhodnya, I.K. (Ed.) *Metallurgy of Arc Welding: Processes in the Arc and Electrode Fusion*; Naukova Dumka: Kiev, Ukraine, 1990; 222p.
24. Sindo, K. *Welding Metallurgy*; Wiley-Interscience; University of Wisconsin: Madison, WI, USA, 1987.
25. Mills, K.C.; Seethharaman, S. *Fundamentals of Metallurgy*; Woodhead Publishing: Abington, UK, 2005.
26. Leskov, G.I. *Electric Welding Arc*; Mashinostroenie: Moscow, Russia, 1970; 335p.
27. Bagryanskiy, K.V. *Theory of Welding Processes*; Vishcha Shkola Publishing House: Kiev, Ukraine, 1976; 424p.
28. Fedko, V.T. Melting and transfer of the electrode metal at arc welding with coated electrodes. *Weld. Int.* **2003**, *2*, 3–10. [CrossRef]
29. Neves, A.C.; Sartori Moreno, J.R.; Corrêa, C.A.; Trevisani Olívio, E.F. Study of arc welding stability in flux cored arc welding process and pulsed continuous current. *Weld. Int.* **2021**, *35*, 158–169. [CrossRef]
30. Bulychev, V.V.; Golubina, S.A.; Latypova, G.R. Prediction of manufacturing process stability in electric arc welding of metals. *Electrometallurgy* **2019**, *8*, 24–29.
31. Lukić, U.; Prokić-Cvetković, R.; Popović, O.; Rajičić, B.; Serbia, B.; Jovičić, R.; Burzić, M. Impact Of Welding Parameters On The Stability Of Gas Metal Arc Welding Process. In Proceedings of the 18th International Research/Expert Conference "Trends in the Development of Machinery and Associated Technology" TMT 2014, Budapest, Hungary, 10–12 September 2014.
32. Guilherme, L.H.; Benedetti, A.V.; Fugivara, C.S.; Magnabosco, R.; Oliveira, M.F. Effect of MAG welding transfer mode on sigma phase precipitation and corrosion performance of 316L stainless steel multi-pass welds. *Integr. Med. Res.* **2020**, *9*, 10537–10549. [CrossRef]
33. Vaz, C.T.; Bracarense, A.Q. The Effect of the Use of PTFE as a Covered-Electrode Binder on Metal Transfer. *Soldag. Insp.* **2013**, *20*, 160–170. [CrossRef]
34. Vaz, C.T. Influência do Polímero Utilizado como Aglomerante em Eletrodos Revestidos Básicos Sobre a Formação de Ferrita Acicular no Metal de Solda. Ph.D. Thesis, Universidade Federal de Minas Gerais, Belo Horizonte, Brazil, 2014.
35. García Rodríguez, A.; Miguel Oria, J.V.; Gómez, A.D. Theoretical and empirical assessment of evaluation methods of the electric charge transference in welding with covered electrodes. *Weld. Int.* **2016**, *30*, 527–534. [CrossRef]
36. Chen, J.H.; Fan, D.; He, Z.Q.; Ye, J.; Luo, Y.C. A study of the mechanism for globular metal transfer from covered. *Weld. J.* **1989**, *68*, 145s–150s.
37. Brandi, S.D.; Taniguchi, C.; Liu, S. Analysis of metal transfer in shielded metal arc welding. *Weld. J.* **1991**, *70*, 261s–270s.
38. Lancaster, J.F. *Metallurgy of Welding*, 5th ed.; Chapman & Hall: London, UK, 1993.
39. Lancaster, J.F. *The Physics of Welding*, 2nd ed.; Pergamon: Oxford, UK, 1986.
40. Ivanov, V.P.; Leshchinskiy, L.K.; Stepnov, K.K. Control of the alloying process of weld metal of variable chemical composition. *Weld. Int.* **2021**, *35*, 441–446. [CrossRef]
41. Letyagin, I.Y. Using Mathematical Modeling To Develop Electrode Coating Composition For Stable Arcing And Arc Restarting. *Solid State Phenom.* **2017**, *265*, 445–449. [CrossRef]
42. Votinova, E.B.; Shalimov, M.P.; Razikov, N.M. Methodology of determination of partial transition coefficients of elements at manual arc welding. *Weld. Diagn.* **2012**, *2*, 28–31.
43. Votinova, E.B.; Shalimov, M.P. Development of the calculation methodology of the weld metal composition at welding with coated electrodes or flux-cored wire. *Weld. Diagn.* **2011**, *5*, 31–36.
44. Il'yaschenko, D.P.; Chinakhov, D.A.; Chinakhova, E.D.; Kirichenko, K.Y.; Verkhoturova, E.V. Assessment Of Negative Influence Of Manganese In Welding Fumes On Welder's Health And Ways To Reduce It. *FME Trans.* **2020**, *48*, 75–81. [CrossRef]
45. Kirichenko, K.Y.; Vakhniuk, I.A.; Rogulin, R.S.; Kirichenko, A.V.; Gridasov, A.V.; Kosyanov, D.Y.; Drozd, V.A.; Piekoszewski, W.; Golokhvast, K.S.; Kholodov, A.S. Characteristics Of Fume Sedimentation In The Working Zone During Arc Welding With Covered Electrodes. *Toxicol. Environ. Chem.* **2019**, *101*, 463–474. [CrossRef]
46. Golovatyuk, A.P.; Sidoruk, V.S.; Levchenko, O.G.; Zatserkovny, S.A.; Taraborkin, L.A. Intensity of aerosols formation at manual welding with modulated current. *Autom. Weld.* **1985**, *2*, 39–40.
47. Il'yashchenko, D.P.; Zernin, E.A.; Shadskii, S.V. Chemical composition of welding aerosol in manual coated electrode arc welding. *Weld. Int.* **2011**, *25*, 719–721. [CrossRef]
48. Gomes, J.F.P.; Albuquerque, P.C.S.; Miranda, R.M.M.; Vieira, M.T.F. Determination of airborne nanoparticles from welding operations. *J. Toxicol. Environ. Health Part A* **2012**, *75*, 747–755. [CrossRef]

49. Belokon, V.M.; Lukyanchikov, I.A.; Dondo, D.A. Movement of Molten Electrode Metal Droplets during Welding in CO_2. *Bull. Belarusian-Russ. Univ.* **2011**, *2*, 6–12. Available online: https://cyberleninka.ru/article/n/dvizhenie-kapel-rasplavlennogo-elektrodnogo-metalla-pri-svarke-v-so2 (accessed on 11 April 2024).
50. Makarenko, V.D.; Shatilo, S.P. Calculation of kinetic characteristics of electrode droplets at their transition through the arc gap in the process of welding with coated electrodes. *Weld. Prod.* **1999**, *14*, 6–10.
51. Kosheleva Natalya, N.; Zakharova Dinara, Z. Application of the Concept "Root of the N-th Degree" in Solving Cubic Equations. *Cardano formula. ANI Pedagog. Psychol.* **2021**, *1*, 162–164. Available online: https://cyberleninka.ru/article/n/primenenie-ponyatiya-koren-n-oy-stepeni-pri-reshenii-kubicheskih-uravneniy-formula-kardano (accessed on 11 April 2024).
52. Ilyashchenko, D.P.; Chinakhov, D.A.; Kirichenko, K.Y.; Sydorets, V.N. Mathematical formula to determine geometrical dimensions of electrode metal droplets transferred with short circuits. *Mater. Sci. Forum* **2018**, *938*, 1–6. [CrossRef]
53. Makarenko, V.D.; Paliy, R.V.; Mukhin, M.Y. *Technological Properties of Assembly Welding of Pipelines*; Makarenko, V.D., Ed.; Nedra-Business Center: Moscow, Russia, 2001; 118p.
54. Belousov Yuriy, V. Calculations of Thermal Processes of the High-Temperature Area of the Surface Heat Sources at Welding. GVUZ "Priazovsky State Technical University". 2000. Available online: https://cyberleninka.ru/article/n/raschety-teplovyh-protsessov-vysokotemperaturnoy-oblasti-poverhnostnyh-istochnikov-teploty-pri-svarke (accessed on 13 April 2024).
55. Ilyashchenko, D.P.; Chinakhov, D.A. Influence of the power source type on heat and mass transfer at manual arc welding. *Weld. Diagn.* **2010**, *6*, 26–29.
56. Gorpenyuk, V.N.; Makarenko, V.D.; Ponomarev, V.E. On the possibility of predicting the porosity in the weld seam with the help of electronic devices when welding with coated electrodes. In *Saving of Material, Energy and Labor Resources in Welding Production*; Publishing House of Chelyabinsk State University: Chelyabinsk, Russia, 1986; pp. 341–342.
57. Górka, J.; Janicki, D.; Fidali, M. Thermographic Assessment of the HAZ Properties and Structure of Thermomechanically Treated Steel. *Int. J. Thermophys.* **2017**, *38*, 183. [CrossRef]
58. Erofeev, V.A.; Strakhova, E.A. Estimation of probability of conformity of weld quality indicators to the specified tolerances in the development of welding technology. *Prep. Ind. Mech. Eng.* **2019**, *17*, 345–349.
59. Sholokhov, M.A.; Melnikov, A.Y.; Buzorina, D.S.; Smorodinsky, Y.G. Development of an approach to forcast the defect formation in the end of a weld joint based on the modeling of heat processes. *Russ. J. Nondestruct. Test.* **2020**, *56*, 460–467. [CrossRef]
60. Filiakov, A.E.; Poloskov, S.I.; Erofeev, V.A.; Sholokhov, M.A. Physical and Mathematical Model of Influence of Deviations of Arc Energy Parameters on Defects Formation at Welding of Pipelines. *Weld. Diagn.* **2020**, *2*, 16–22.
61. Yapp, D.; Blackman, S.A. Recent Developments in High Productivity Pipeline Welding. *J. Braz. Soc. Mech. Sci. Eng.* **2004**, *26*, 89–97. [CrossRef]
62. Makarenko, V.D.; Muravyev, K.A.; Kalyanov, A.I. Features of manual arc welding of root seams of non-rotating joints of oil pipelines operated in Western Siberia. *Weld. Prod.* **2005**, *12*, 38–41.
63. Ilyaschenko, D.P.; Kryukov, A.V.; Lavrova, E.V.; Kuznetsov, M.A.; Verkhoturova, E.V. Determination of Parameters of Electrode Metal Transported Drops by Simulation and Visualization. *Devices Methods Meas.* **2020**, *11*, 222–227. [CrossRef]
64. Ilyashchenko, N.V.P. Certificate of Registration of Computer Programs No. 2015615010. Calculation of Heat Deposition in a Drop of Electrode Metal at RDS/D.P. 6 May 2015. Available online: https://portal.tpu.ru/portal/pls/portal/docs/1/16047790.JPEG (accessed on 14 June 2024).
65. Ilyashchenko, D.P.; Pavlov, N.V.; Chinakhov, D.A. Comparative analysis of heat distribution in the product at fusion arc welding. *Repair Restor. Mod.* **2011**, *3*, 35–37.
66. Chinakhov, D.A.; Il'yashchenko, D.P. The Influence of Two-Jet Gas Shielding Parameters on the Structure and Microhardness of Steel 45 Joints during Consumable Electrode Welding. *Metals* **2023**, *13*, 1136. [CrossRef]
67. Marques, E.S.V.; Silva, F.U.G.; Pereira, A.B. Comparison of finite element methods in fusion welding processes-a review. *Metals* **2020**, *10*, 75. [CrossRef]
68. Sapozhkov, S.B.; Zernin, E.A.; Petrova, E.D.; Petrov, R.V.; Zakharov, M.A. Application of Nano- and Ultradisperse Materials for Control of Structure and Properties of Metals in Joining Technologies: World Practice (Review). Vestnik NovSU. 2023. Available online: https://cyberleninka.ru/article/n/primenenie-nanoi-ultradispersnyh-materialov-dlya-upravleniya-strukturoy-i-svoystvami-metallov-v-soedinitelnyh-tehnologiyah-mirovaya (accessed on 13 April 2024).
69. Ilyashchenko, D.P.; Chinakhov, D.A.; Verkhoturova, E.V.; Lavrova, E.V. Stability Of MMA Welding With Protective Coatings. *Struct. Integr. Life* **2020**, *20*, 33–36.
70. Rybin, V.S.; Scherbakov, I.A. Model of welding thermal processes with a limited number of fictitious point sources. Ferrous metallurgy. *Bull. Sci.-Tech. Econ. Inf.* **2022**, *78*, 435–444.
71. Sheshukov, O.Y.; Nekrasov, I.V.; Metelkin, A.A.; Lozovaya, E.Y.; Shevchenko, O.I.; Savelyev, M.V. *Modern Steel: Theory and Technology*; Textbook: Recommended by the Methodical Council of the Ural Federal University for Students of the University, Studying in the Fields of Training 22.03.02, 22.04.02—Metallurgy; Mironova, M.V., Ed.; Nizhny Tagil Technological Institute (branch) of UrFU: Nizhny Tagil, Russia, 2020; 400p, Available online: https://elar.urfu.ru/handle/10995/94364 (accessed on 14 June 2024).
72. Panteleenko, F.I.; Mamonov, A.M. Installation for low-deformation welding of stainless steels with dry ice. *Foundry Prod. Metall.* **2022**, *2*, 54–58. [CrossRef]

73. Mamadaliev, R.A.; Bakhmatov, P.V.; Martyushev, N.V.; Skeeba, V.Y.; Karlina, A.I. Influence Of Welding Regimes On Structure And Properties Of Steel 12kh18n10t Weld Metal In Different Spatial Positions. *Metallurgist* **2022**, *65*, 1255–1264.
74. Vicente, A.A.; Silva AC, S.; Torres Lopez, E.A.; Pereira, M.; Santos, T.F.; Tenório, J.A. The possible solidification modes of austenitic stainless steels joints according to different chemical compositions and cooling rates. *Weld. Int.* **2024**, *38*, 187–197. [CrossRef]
75. Mamadaliev, R.A.; Bakhmatov, P.V. Distribution of alloying elements in multi-pass welds of chromium-nickel steel. *Met. Heat Treat. Met.* **2023**, *5*, 55–60.
76. Bakhmatov, P.V.; Mamadaliev, R.A.; Kravchenko, A.S. Change in weld metal structure and properties for multi-pass butt welding of stainless steel process piping. In *Current Problems and Ways of Industry Development: Equipment and Technologies*; Springer: Cham, Switzerland, 2021; pp. 497–506.
77. Malhotra, D.; Shahi, A.S. Weld metal composition and aging influence on metallurgical, corrosion and fatigue crack growth behavior of austenitic stainless steel welds. *Mater. Res. Express* **2019**, *6*, 106555. [CrossRef]
78. Zhang, T.; Yu, H.; Li, Z.; Kou, S.; Kim, H.J.; Tillmann, W. Progress on effects of alloying elements on bainite formation and strength and toughness of high strength steel weld metal. *Mater. Res. Express* **2021**, *8*, 032002. [CrossRef]
79. Krivonosova, E.A.; Akulova, S.N.; Myshkina, A.V. To the problem of corrosion damage of welded seams. Bulletin of Perm National Research Polytechnic University. Mechanical Engineering. *Mater. Sci.* **2017**, *19*, 118–119.
80. Krivonosova, E.A. Predicting the properties of the metal of welded joints on the basis of the results of quantitative parametrisation of the structure. *Weld. Int.* **2016**, *30*, 459–462. [CrossRef]
81. Krivonosova, E.A. Prediction of weld metal properties based on the results of quantitative structure parameterization. *Weld. Prod.* **2015**, *6*, 3–6.
82. Matvienko, Y.G.; Vasiliev, I.E.; Chernov, D.V.; Marchenkov, A.Y. Diagnostics of welded joints in main pipelines equipment. *Sci. Technol. Oil Prod. Pipeline Transp.* **2018**, *8*, 618–630.
83. AMelakhsou, A.; Batton-Hubert, M. On welding defect detection and causalities between welding signals. In Proceedings of the 2021 IEEE 17th International Conference on Automation Science and Engineering (CASE), Lyon, France, 23–27 August 2021; pp. 401–408. [CrossRef]
84. Sholokhov, M.A.; Buzorina, D.S.; Lunina, E.V. Efficiency of operation of inverter rectifier power supplies. *Weld. Diagn.* **2012**, *3*, 26–29.